Collision-resolved pressure sensing

Daniel S. Barker,[1,*] Daniel Carney,[2,†] Thomas W. LeBrun,[3] David C. Moore,[4] and Jacob M. Taylor[5]

[1] *Sensor Science Division, National Institute of Standards and Technology, Gaithersburg, MD*
[2] *Physics Division, Lawrence Berkeley National Laboratory, Berkeley, CA*
[3] *Microsystems and Nanotechnology Division, National Institute of Standards and Technology, Gaithersburg, MD*
[4] *Wright Laboratory, Department of Physics, Yale University, New Haven, CT*
[5] *Joint Quantum Institute, University of Maryland, College Park, MD*

(Dated: August 8, 2024)

While a continuous Brownian description of noise from heat and pressure is adequate to model measurements with relatively long integration times, these forces are ultimately generated by quantized degrees of freedom like phonons and gas particles. Fundamentally, the ultimate limit of this sensing problem is to resolve all of the individual system-sensor collisions. Here, we propose the use of nanomechanical devices operated with impulse readout sensitivity around the "standard quantum limit" to sense ultra-low gas pressures by directly counting the individual collisions of gas particles on a sensor. We illustrate this in two paradigmatic model systems: an optically levitated nanobead and a tethered membrane system in a phononic bandgap shield.

I. INTRODUCTION

Mechanical objects placed in imperfect vacuum are subject to heat and pressure from their environments. While measurements of the motion of the mechanical object over long timescales will detect these thermal backgrounds as continuous random Brownian motion of the system [1, 2], measurements at very fast timescales can be sensitive to the individual microscopic system-environment interactions [3–5], a regime in which the continuous Brownian description breaks down. In this paper, we suggest methods to detect the individual gas collisions with a mechanical sensing element, representing the fundamental quantum limit of pressure sensing, using detectors operated at or near the quantum readout regime [6–9].

A key application of this idea is the development of primary pressure sensors capable of operating in the ultra-high vacuum (UHV, 10^{-9} Pa $< P \leq 10^{-6}$ Pa) and extreme-high vacuum (XHV, $P \leq 10^{-9}$ Pa [10]), an open frontier in precision metrology [11, 12]. This level of environmental isolation is of increasing importance in a diverse array of contexts. Precision tests of general relativity and quantum mechanics are expected to be limited by background gas collisions even well into the XHV regime, thus requiring ultra-precise pressure measurements to characterize the resulting systematic uncertainties [13–17]. In trapped-ion quantum computing, gas pressure at the UHV level fundamentally limits computations beyond about 50 qubits due to scattering with the ions [18]; to scale these systems as well as to implement error correction protocols, a detailed measurement of the gas collision spectra at XHV will be needed [19]. In the search for dark matter, detection of individual gas collisions will be required to calibrate backgrounds in many searches for dark matter with masses below 100 MeV/c^2 [20–22]; characterizing the low momentum tail of the distribution of gas collisions could enable searches for dark matter masses as low as 1 MeV/c^2 to be performed [23].

Pressure gauges currently serving the UHV and XHV ranges have significant drawbacks. Ionization gauges have sensitivity that drifts substantially in time; are highly sensitive to external magnetic fields; and employ a hot filament, which perturbs the vacuum environment [24]. In accelerator facilities, gravitational wave detectors, quantum computers, and optical clocks, the limitations of ionization gauges lead to increased system down-time, difficulty in leak detection, smaller qubit count, and poorly characterized systematics, respectively. Recently developed cold-atom vacuum standards are primary pressure sensors that offer excellent stability and accuracy [25]. However, they suffer from extremely slow and intermittent readout, due to small atom-molecule scattering cross-sections and the need to periodically reload the atom trap, respectively [12, 25]. The non-destructive mechanical sensors we propose here offer a complementary technique that allows fast, real-time, non-perturbative, primary pressure sensing.

To estimate the regime where the continuous thermal noise model breaks down, consider a small mechanical element of mass m_s and cross-sectional area A in a dilute ideal gas with pressure P and temperature $T_{\rm gas}$. The ambient gas particles, with mass m_g, collide with the sensor and impart momentum kicks of order $\Delta p_T \approx \sqrt{m_g k_B T_{\rm gas}}$. These kicks occur at an average rate of order

$$\Gamma = \frac{PA}{\Delta p_T} \approx 3 \text{ Hz} \times \left(\frac{P}{10^{-10} \text{ Pa}}\right)\left(\frac{A}{0.1\ \mu\text{m}^2}\right). \quad (1)$$

In the low pressure, small sensor regime, we see this rate can be on the order of one to 100 collisions per second. Here, we used the Boltzmann distribution to compute the typical velocity of the gas particles, taken to be diatomic hydrogen $m_g \approx 2$ u at room temperature $T = 300$ K. To resolve such a kick, the sensor needs to be operated with

* daniel.barker@nist.gov
† carney@lbl.gov

sensitivity $\Delta p \lesssim \Delta p_T \approx 7$ keV/c and with a bandwidth $1/\tau > \Gamma$ where τ is the integration time for a measurement of a single kick.

We now ask: can these weak kicks be resolved by a macroscopic sensor? One simple answer is given by comparing with the standard quantum limit (SQL) for impulses [26, 27],

$$\Delta p_{\rm SQL} = \sqrt{\frac{\hbar m_s}{\tau}} \approx 0.8 \text{ keV}/c \times \left(\frac{m_s}{1 \text{ fg}}\right)^{1/2} \left(\frac{1 \text{ ms}}{\tau}\right)^{1/2}. \quad (2)$$

The sensor mass m_s in this example is benchmarked against a 50 nm radius silica sphere for comparison with (1). As discussed below, measurements at this SQL level have been achieved to good approximation in a number of nanomechanical devices [28, 29]. Taken together, these numbers indicate that quantum-limited nanomechanical devices monitored for impulses at sub-second integration times and with near-SQL sensitivity, could be sensitive to discrete kicks from the ambient gas in UHV and XHV environments [23, 27, 30].

In what follows, we provide more detailed calculations and proposals toward achieving such measurements. Our primary concern will be on feasibility of achieving the relevant limits above, especially the bandwidth requirements: the quantum noise (2) scales favorably $\Delta p_{\rm SQL} \sim 1/\sqrt{\tau}$ with longer measurement time, but this must be balanced against common technical noise sources with approximately flat power, which lead to $\Delta p_{\rm tech} \sim \sqrt{\tau}$.

II. SENSOR CONCEPT AND DESIGN

We will consider opto- or electro-mechanical devices operated as impulse sensors. These devices consist of a mode of a mechanical element of mass m_s, which we approximate as executing harmonic motion at frequency ω_s, continuously monitored by an optical or microwave field. Typically one monitors the position $x(t)$ of the mechanics; assuming we have knowledge of the linear response of the device to an input force, we can infer the applied force time series $F(t)$.

First, consider optically monitoring the center-of-mass motion $x(t)$ of a levitated dielectric bead [31–33]. See Fig. 1, left. Levitation of dielectric beads with radii ranging from 50 nm to 10 μm and oscillation frequencies in the 0.1 kHz to 1 MHz range has been demonstrated. In particular, very recently, a pair of experiments have demonstrated feedback cooling to the center-of-mass ground state in optically levitated beads with radius around 100 nm, trapped at around $\omega_s/2\pi \approx 100$ kHz [28, 29]. This feedback cooling mechanism operates by continuously monitoring the bead's position fluctuations and applying feedback kicks in order to drive it to the ground state. To reach the ground state this way requires precisely that one can monitor the fluctuations near the SQL, corresponding to the ground state uncertainty $\Delta x_{SQL} = \sqrt{\hbar/m_s\omega_s}$ of the mass. Thus these systems are already operating in the SQL regime, although at two orders of magnitude higher frequency than the optimal integration time assumed in (2). Even at this sensitivity, they should be capable of sensing the high-energy tail of the Boltzmann distribution [30].

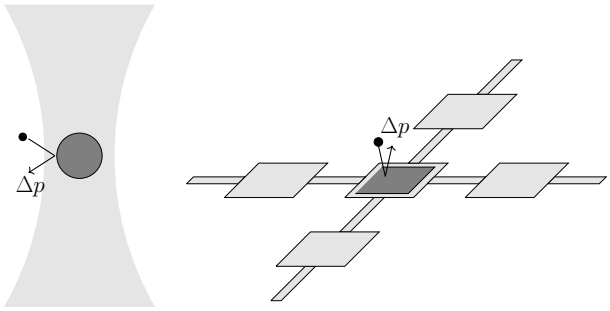

FIG. 1. Schematics of the basic detection scheme, with either a levitated nanoparticle or tethered membrane in the unit cell of a phononic bandgap shield [34, 35]. When an environmental gas particle collides with the mechanical element, it deposits momentum Δp, which can be detected by continuously monitoring the position $x(t)$ of the element.

Alternatively, one could consider a tethered system like a membrane. In this approach, one monitors the amplitude of the vibrations [36], for example of the first transverse vibrational mode in the geometry of Fig. 1. For example, an atomically-thin membrane made from graphene [37] or a non-conductive material like silicon nitride [38, 39] around 20 nm on each side would have a mass around $m_s \approx 10^{-3}$ fg, and thus could achieve the required sensitivity if its fundamental mode could be tuned to around $\omega_s/2\pi \approx 10$ MHz. Such a small membrane would have to be read out capacitively [37]; alternatively, a larger ($\sim \mu$m-scale) membrane operated at lower ($\sim$ kHz) frequencies could also be used in the optical domain.

The collision of a gas particle with the mechanical sensing element can be modeled as a sharp impulse

$$F_{\rm sig}(t) \approx \Delta p \delta(t - t_0), \quad (3)$$

where for example a typical gas collision will have $\Delta p \approx \Delta p_T = \sqrt{m_g k_B T_{\rm gas}}$. In the measured position data $x(t)$, such an impulse will appear as a kick followed by a ring-down. Individual collisions can be resolved if the size Δp of these kicks is large compared to the continuous noise acting on the device. We model this noise, which comes both from the quantum-limited readout as well as any technical noise sources, as an additional net force $F(t) = F_{\rm sig}(t) + F_{\rm noise}(t)$, which leads to an uncertainty

$$\Delta p^2_{\rm noise} = \Delta p^2_{\rm SQL} + \Delta p^2_{\rm tech}. \quad (4)$$

The first term is the quantum readout noise, given in Eq. (2), and assuming that $\tau \lesssim 1/\omega_s$; for even longer integration times, one should replace $\tau \to 1/\omega_s$.

The second term encapsulates any additional "technical" noises, typically modeled as Johnson-Nyquist noise $\Delta p_{\rm tech} = \sqrt{4 m_s k_B T_{\rm noise} \gamma_s \tau}$ at some effective bath temperature $T_{\rm noise}$, where $\gamma_s = \omega_s/Q$ is the effective damping rate and Q is the mechanical quality factor [9, 27]. Taking the integration time $\tau \sim 1/\omega_s$, i.e., measuring for roughly one oscillation time, we have

$$\Delta p^2_{\rm noise} = \hbar m_s \omega_s \left[1 + \frac{4 k_B T_{\rm noise}}{\hbar \omega_s Q}\right]. \tag{5}$$

To achieve the SQL (2), we see that we need a sufficiently high-Q oscillator. Note that with $\tau \sim 1/\omega_s$ and an oscillator above a few Hz, comparing to the expected event rate (1), we can resolve the collisions event-by-event.

In the example of a levitated bead, the required Q values and resulting impulse sensitivity has been demonstrated in practice [28, 29, 40]. Thus, with these systems, it should be immediately possible to detect collisions with SQL-level thresholds (2) and event-by-event integration times fast enough to resolve each individual collision in (1). In a membrane system, the same approach may be more challenging due to the presence of a phononic bath from the surrounding substrate. To see an individual gas collision, we require that the heating from these phonons is subdominant to the collision signal:

$$\frac{\Delta p_T}{\Delta p_{\rm tech}} = \sqrt{\frac{m_g T_{\rm gas}}{m_s T_{\rm noise}} \frac{Q}{\omega_s \tau}} \gtrsim 1, \tag{6}$$

where $Q = \gamma_s/\omega_s$ is the quality factor of the membrane mode. Again with an integration window $\tau \approx 1/\omega_s$, and with the same graphene monolayer parameters given above ($m_s \sim 10^{-3}$ fg, corresponding to roughly 400 nm^2 active area), detecting the $T_{\rm gas} \approx 4$ K helium atoms boiling off the walls of a dilution refrigerator $T_{\rm noise} \approx 10$ mK would require $Q \sim 10^5$. This could potentially potentially be obtained with phononic bandgap shielding [34, 35], as depicted schematically in Fig. 1. We note also that with sufficiently fast measurements ($\tau \lesssim Q/\hbar k_B T_{\rm noise}$) one could try to resolve individual thermal phonons rather than treat them as a continuous background, relevant for example in searches for light dark matter scattering with solid-state phonons [41].

III. GAS COLLISION SPECTRUM

Above, we outlined the basic sensitivity of a mechanical sensor to individual gas collisions which deposit a given impulse Δp. In a real gas, collisions of ambient gas with a mechanical sensor produce a spectrum of impulse signals. To understand how to use our mechanical sensors as gauges for pressure or for identification of gas species, we need to be more precise about the expected signal distribution.

The thermal de Broglie wavelength of the typical gas of interest is much smaller than the nm-scale devices discussed here, so we can treat the gas-sensor collisions classically. The background gas can scatter off the mechanical sensor both specularly (perfectly reflectively) as well as diffusely (thermalizing with the sensor surface) [42–45]. We can model both specular and diffuse scattering to derive a differential event rate in terms of the momentum transfer in each event:

$$\frac{d\Gamma}{d\Delta p} = \frac{n_g A \Delta p}{4 m_g^2} f_{\rm B}\left(\frac{\Delta p}{2 m_g}\right)\left[(1-\alpha) + \alpha\, \xi\left(\frac{\Delta p}{m_g \overline{v}}\right)\right]. \tag{7}$$

Here, n_g is the number density of the gas with mass m_g, A is the surface area of the sensor, $f_{\rm B}(v)$ is the Boltzmann distribution for velocity v at temperature $T_{\rm gas}$, and $\overline{v} = \sqrt{k_B T_{\rm gas}/m_g}$ is the root-mean-square thermal velocity. The overall factor before the brackets in (7) represents specular reflection. We include a phenomenological coefficient $0 \le \alpha \le 1$ that parametrizes the fraction of scattering events which are diffuse, whose spectrum is modified by the $\mathcal{O}(1)$ factor

$$\xi(x) = \sqrt{\pi} x \left(1 - \frac{2}{x^2}\right) \mathrm{erf}\left(\frac{x}{2}\right) e^{-x^2/8} + 2 e^{-3x^2/8}. \tag{8}$$

Here $x = \Delta p/m_g \overline{v}$ is a dimensionless measure of the momentum transfer, and erf is the Gaussian error function. The coefficient α can in principle be calculated microscopically, measured, or mitigated, as we discuss below.

An example of this spectrum is plotted in Fig. 2. For brevity, equations (7) and (8) make the simplifying assumption that the sensor surface and gas are at the same temperature. In Appendix B and Appendix C, we show that corrections from out-of-equilibrium effects lead to easily tolerable errors in the measurements outlined below even with very large temperature differentials.

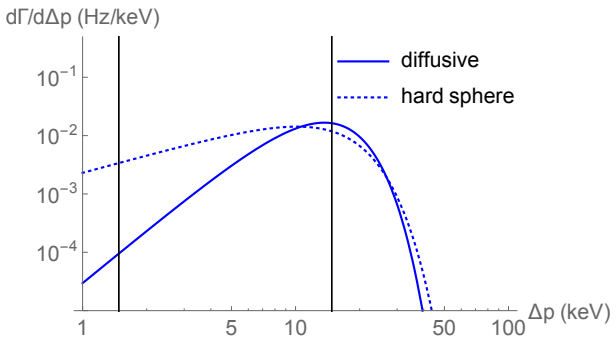

FIG. 2. Example spectrum of collision events, expressed as a differential rate $d\Gamma$ per given impulse value Δp. The black lines label the nominal detection threshold $\Delta p_{\rm min} = \Delta p_{\rm SQL}$, with a solid sphere of radius 50 nm, trapped at either $\omega_s/2\pi =$ 1 kHz (left) or 100 kHz (right). We again assume the gas is dominated by diatomic hydrogen at 300 K, and we show the predictions for pure hard sphere scattering (specular) as well as diffusive scattering corrections.

IV. APPLICATION TO PRIMARY PRESSURE SENSING

Prior mechanical vacuum sensors have been based on damping measurements, which operate in the regime where the readout is much slower than the typical gas collision rate (1), and therefore limited to the high vacuum range (HV, 10^{-6} Pa $\leq P < 10^{-1}$ Pa) [45–48]. Here, we explain how direct detection of background gas molecules through collision counting allows primary pressure sensing in the UHV and XHV regimes using mechanical systems [11].

To use our collision-resolved sensor as a pressure gauge, we want to monitor the total number of gas collisions above some threshold $\Delta p_{\rm min}$ (for example, $\Delta p_{\rm SQL}$) in a fixed time interval; detailed measurement of the individual momentum transfers is not crucial. The total detectable event rate $\Gamma(\Delta p_{\rm min})$ can be derived from (7) by integrating from our detection threshold $\Delta p_{\rm min}$ to infinity. This gives

$$\Gamma(\Delta p_{\rm min}) = \frac{n_g A \overline{v}}{\sqrt{2\pi}}\Big[(1-\alpha)\eta_s\Big(\frac{\Delta p_{\rm min}}{m_g \overline{v}}\Big) + \alpha\,\eta_d\Big(\frac{\Delta p_{\rm min}}{m_g \overline{v}}\Big)\Big], \tag{9}$$

where the detectable momentum cutoffs for specular scattering η_s and diffuse scattering η_d are given by

$$\begin{aligned}\eta_s(x_{\rm min}) &= e^{-x_{\rm min}^2/8}\\ \eta_d(x_{\rm min}) &= e^{-x_{\rm min}^2/2} + \frac{\sqrt{\pi}}{2} x_{\rm min}\,\mathrm{erf}\left(\frac{x_{\rm min}}{2}\right) e^{-x_{\rm min}^2/4}.\end{aligned} \tag{10}$$

In (10), $x_{\rm min} = \Delta p_{\rm min}/m_g\overline{v}$. Eq. (9) assumes detectability of impulses on all three spatial axes; if one is monitoring only one or two axes there is an additional geometric factor (see Appendix A). Now, using the ideal gas law and inverting Eq. (9), we find an expression for the pressure:

$$P = \Gamma(\Delta p_{\rm min})\frac{\sqrt{2\pi} k_B T_{\rm gas}}{A\overline{v}[(1-\alpha)\eta_s(x_{\rm min}) + \alpha\eta_d(x_{\rm min})]}. \tag{11}$$

This gives an estimate of the gas pressure in terms of the measured event rate $\Gamma(\Delta p_{\rm min})$.

Eq. (11) contains two constants (k_B and m_g) and three measured quantities ($\Gamma(\Delta p_{\rm min})$, A, and $T_{\rm gas}$). It is therefore traceable to the second, meter, kilogram, and kelvin. The rate Γ can be measured as discussed above. The surface area of a nanosphere can be determined by combining an *in-situ* mass measurement with prior scanning electron microscope characterization [49]; the area of a tethered device can be set using lithography and then measured using atomic force microscopy. The gas temperature can be measured with calibrated or primary contact thermometers [50] mounted on the exterior of the vacuum chamber, a standard technique in pressure metrology [25].

The remaining difficulty is the unknown accommodation coefficient α. However, the dependence on α in (11) drops out when the optomechanical system detects all background gas collisions (η_s, $\eta_d \to 1$; i.e., when $\Delta p_{\rm min} \to 0$). As discussed in detail in Appendix C, we estimate that $\eta_s > 0.9$ is sufficient for better than 5 % total uncertainty; this is satisfied when $\Delta p_{\rm min} \approx 6.3$ keV/c for H_2 at 300 K. State-of-the-art total uncertainty < 2 % would be achievable with $\eta_s > 0.95$, which corresponds to $\Delta p_{\rm min} \approx 4.4$ keV/c for H_2 gas at 300 K. All told, assuming the measurement of $\Gamma(\Delta p_{\rm min})$ is limited by molecule arrival shot noise, the nanosphere sensor plotted in Fig. 2 would average down statistical uncertainty approximately 100 times faster than a deployable, primary cold-atom vacuum sensor, due to its increased event rate [12].

V. APPLICATION TO GAS ANALYSIS

As another possible application, we could use more details of the collision spectrum to deduce the fraction of different gas species present. With multiple species, the differential event rate becomes

$$\frac{d\Gamma}{d\Delta p} = \sum_i \frac{n_{g,i} A \Delta p}{4 m_{g,i}^2} f_{\rm B}\Big(\frac{\Delta p}{2m_{g,i}}\Big)\Big[(1-\alpha) + \alpha\,\xi\Big(\frac{\Delta p}{m_{g,i}\overline{v}_i}\Big)\Big], \tag{12}$$

where the sum runs over all background gas species i. Because the peak event rate due to gas i occurs roughly at $\Delta p = 2m_{g,i}\overline{v}_i$, we can use measurements of the differential event rate at several resolvable momenta Δp to extract all background gas densities $n_{g,i}$. Fully disentangling the overlapping event distributions requires detailed knowledge of the characteristic momentum spectrum of each gas; we give details on this procedure in Appendix D.

Such a collision counting gas analyzer has significant advantages over conventional quadrupole mass spectrometers. First, it is primary, allowing gas analysis in applications were periodic calibrations are difficult. Second, it is intrinsically low outgassing, permitting analysis deep in the XHV, where current spectrometers may add large systematic uncertainty. Finally, its active area is at most millimeter sized, so (with further advances in meta-optics and nanophotonics [51]) leak detection could be performed in compact, autonomous systems.

VI. OUTLOOK

In a sufficiently good vacuum, the only way to sense ambient gas pressure is to detect individual gas collisions with a sensor. We outlined two architectures for such detection using mechanical sensors operated in the quantum readout regime, which would enable a pressure standard capable of operation in the increasingly important XHV range. Such collision counters would represent pressure sensing at its fundamental limit, where the

concept of continuous pressure breaks down, requiring a description in terms of individual quanta.

ACKNOWLEDGMENTS

We thank Stephen Eckel, James Fedchak, Sinead Griffin, Lorenzo Magrini, Archana Raja, Cindy Regal, Benjamin Reschovsky, Alp Sipahigil, and Dalziel Wilson for discussions. DC is supported by the US Department of Energy under contract DE-AC02-05CH11231 and Quantum Information Science Enabled Discovery (QuantISED) for High Energy Physics grant KA2401032. DCM is supported, in part, by NSF Grant PHY-2109329 and ONR Grant N00014-23-1-2600.

Appendix A: Detailed collision spectrum calculations

We determine the collision spectrum using the kinetic theory of gases. The number of molecular collisions with the sensor surface element dA in time element dt that have incoming velocity $\vec{v}_i$ and outgoing velocity $\vec{v}_o$ is [43, 44]

$$d^8N_c(\vec{v}_i,\vec{v}_o) = n_g\,dA\,dt\left(\frac{1}{2\pi\overline{v}^2}\right)^{3/2} v_i\cos\theta_i\, e^{-v_i^2/2\overline{v}^2} \times \frac{1}{2\pi\overline{v}^4} v_o\cos\theta_o\; e^{-v_o^2/2\overline{v}^2}\; d\vec{v}_i d\vec{v}_o, \tag{A1}$$

where n_g is the gas density; $v_{i,o}$ is the magnitude of $\vec{v}_{i,o}$; $\overline{v} = \sqrt{k_B T_{\rm gas}/m_g}$ is the root-mean-square thermal velocity of the gas with temperature $T_{\rm gas}$ and mass m_g; and $\theta_{i,o}$ is the polar angle between $\vec{v}_{i,o}$ and the surface normal $\hat{u}_\perp$. Equation (A1) assumes that the gas molecules scatter diffusely from the sensor surface according to the cosine law after thermalizing with it (see Refs. [42–45]) and that the sensor is in thermal equilibrium with the gas. We consider the possibility that the sensor is not in thermal equilibrium with the gas, which may occur at low background pressure or high optical power [52], in Appendix B.

To find the number of collisions that impart momentum Δp perpendicular to the surface, we integrate Eq. (A1) subject to the constraint $\vec{v}_o.\hat{u}_\perp + \vec{v}_i.\hat{u}_\perp - \Delta p/m_g = 0$. After transforming to Cartesian coordinates, we have

$$d^3N_c(\Delta p) = n_g\,dA\,dt\left(\frac{1}{2\pi\overline{v}^2}\right)^{3/2}\int_0^{\Delta p/m_g} dv_{i,z} \times \iint_{-\infty}^{\infty} dv_{i,x}dv_{i,y}\, v_{i,z}\, e^{-(v_{i,x}^2+v_{i,y}^2+v_{i,z}^2)/2\overline{v}^2} \times \frac{1}{2\pi\overline{v}^4} dv_{o,z} \iint_{-\infty}^{\infty} dv_{o,x}dv_{o,y}\, v_{o,z}\, e^{-(v_{o,x}^2+v_{o,y}^2+v_{o,z}^2)/2\overline{v}^2}, \tag{A2}$$

where $v_{i,z} = \vec{v}_i.\hat{z}$ (with $\hat{z} = \hat{u}_\perp$ the unit vector defining the z axis) and so on for the other Cartesian components of $\vec{v}_i$ and $\vec{v}_o$. We impose the momentum transfer constraint by taking $v_{o,z} = \Delta p/m_g - v_{i,z}$ and $dv_{o,z} = d\Delta p/m_g$. Evaluating the integrals over the plane parallel to the surface then yields

$$d^3N_c(\Delta p) = \frac{n_g\,dA\,dt}{\overline{v}^2}\left(\frac{1}{2\pi\overline{v}^2}\right)^{1/2}\frac{d\Delta p}{m_g} \times \int_0^{\Delta p/m_g} dv_{i,z}\, v_{i,z}(\Delta p/m_g - v_{i,z})\, e^{-\left(v_{i,z}^2+\left(\frac{\Delta p}{m_g}-v_{i,z}\right)^2\right)/2\overline{v}^2}. \tag{A3}$$

The integral in Eq. (A3) can be solved by completing the square and mapping onto known Gaussian integrals. The result is

$$\sqrt{\pi}e^{-\Delta p^2/4m_g^2\overline{v}^2}\left[\frac{1}{\sqrt{\pi}}\left(\frac{v_{i,z}\overline{v}^2}{2} - \frac{\Delta p\overline{v}^2}{4m_g}\right)e^{-\left(v_{i,z}/\overline{v}-\Delta p/2m_g\overline{v}\right)^2} + \frac{1}{2}\left(\frac{\Delta p^2\overline{v}}{4m_g^2} - \frac{\overline{v}^3}{2}\right)\left(1+\mathrm{erf}\left(v_{i,z}/\overline{v} - \Delta p/2m_g\overline{v}\right)\right)\right]_0^{\Delta p/m_g}, \tag{A4}$$

where erf is the Gaussian error function. Inserting Eq. (A4) into Eq. (A3) gives the number of collisions imparting momentum Δp per unit area per unit time

$$\frac{d^3N_c(\Delta p)}{dA\,dt} = n_g\frac{d\Delta p}{m_g}\left(\frac{1}{2\pi\overline{v}^2}\right)^{1/2}\left(\frac{\Delta p}{2m_g}e^{-\Delta p^2/2m_g^2\overline{v}^2} + \frac{\sqrt{\pi}}{2}\left(\frac{\Delta p^2}{2m_g^2\overline{v}} - \overline{v}\right)\mathrm{erf}\left(\Delta p/2m_g\overline{v}\right)e^{-\Delta p^2/4m_g^2\overline{v}^2}\right). \tag{A5}$$

If we rearrange Eq. (A5) and integrate over the sensor area, we find the differential event rate

$$\frac{d\Gamma}{d\Delta p} = \frac{n_g A\Delta p}{4m_g^2}\left(\frac{1}{2\pi\overline{v}^2}\right)^{1/2} e^{-\Delta p^2/8m_g^2\overline{v}^2}\left(2e^{-3\Delta p^2/8m_g^2\overline{v}^2} + \frac{\sqrt{\pi}}{2}\left(\frac{2\Delta p}{m_g\overline{v}} - \frac{4m_g\overline{v}}{\Delta p}\right)\mathrm{erf}\left(\Delta p/2m_g\overline{v}\right)e^{-\Delta p^2/8m_g^2\overline{v}^2}\right) = \frac{n_g A\Delta p}{4m_g^2}\left(\frac{1}{2\pi\overline{v}^2}\right)^{1/2} e^{-\Delta p^2/8m_g^2\overline{v}^2}\xi\left(\frac{\Delta p}{m_g\overline{v}}\right) \tag{A6}$$

where $\Gamma = dN_c/dt$ is the total collision rate and the diffuse scattering correction $\xi(\Delta p/m_g\overline{v})$ is the term in

parentheses on the first line of the equation. Taking $\xi(\Delta p/m_g\overline{v}) \to 1$ yields the differential event rate for elastic scattering. If we note that the Maxwell-Boltzmann distribution for $\Delta p/2m_g$ is $f_B(\Delta p/2m_g) = e^{-\Delta p^2/8m_g^2\overline{v}^2}/\sqrt{2\pi\overline{v}^2}$ and include momentum accommodation, then Eq. (A6) becomes Eq. (7) in the main text.

We calculate the total detectable collision rate by integrating Eq. (A6) over Δp from $\Delta p_{\rm min}$ to ∞, where $\Delta p_{\rm min}$ is the momentum transfer that corresponds to a measurement signal-to-noise ratio of 1 (or a chosen cutoff to ensure no spurious events). Carrying out the integration yields

$$\begin{aligned}\Gamma\big|_{\Delta p>\Delta p_{\rm min}} &= \frac{n_g A}{2}\left(\frac{1}{2\pi\overline{v}^2}\right)^{1/2}\left(\overline{v}^2 e^{-\Delta p_{\rm min}^2/2m_g^2\overline{v}^2} + \frac{\sqrt{\pi}}{2}\int_{\Delta p_{\rm min}}^{\infty}\frac{d\Delta p}{m_g}\left(\frac{\Delta p^2}{m_g^2\overline{v}} - 2\overline{v}\right)\mathrm{erf}\big(\Delta p/2m_g\overline{v}\big)e^{-\Delta p^2/4m_g^2\overline{v}^2}\right)\\ &= \frac{n_g A}{2}\left(\frac{1}{2\pi\overline{v}^2}\right)^{1/2}\left(2\overline{v}^2 e^{-\Delta p_{\rm min}^2/2m_g^2\overline{v}^2} + \frac{\sqrt{\pi}\Delta p_{\rm min}\overline{v}}{m_g}\mathrm{erf}\big(\Delta p_{\rm min}/2m_g\overline{v}\big)e^{-\Delta p_{\rm min}^2/4m_g^2\overline{v}^2}\right).\end{aligned} \tag{A7}$$

If we rewrite Eq. (A7) in terms of the expected total collision rate, we get

$$\Gamma\big|_{\Delta p>\Delta p_{\rm min}} = \frac{n_g A\overline{v}}{\sqrt{2\pi}}\eta_d(\Delta p_{\rm min}), \tag{A8}$$

with

$$\eta_d(\Delta p_{\rm min}) = \left(e^{-\Delta p_{\rm min}^2/2m_g^2\overline{v}^2} + \frac{\sqrt{\pi}\Delta p_{\rm min}}{2m_g\overline{v}}\mathrm{erf}\big(\Delta p_{\rm min}/2m_g\overline{v}\big)e^{-\Delta p_{\rm min}^2/4m_g^2\overline{v}^2}\right), \tag{A9}$$

which defines the detectable momentum cutoff for diffuse scattering $\eta_d(\Delta p_{\rm min}) < 1$. The detectable momentum cutoff for specular scattering is $\eta_s(\Delta p_{\rm min}) = e^{-\Delta p_{\rm min}^2/8m_g^2\overline{v}^2}$, which can be found by taking the $\xi(\Delta p/m_g\overline{v}) \to 1$ limit in Eq. (A6) and then carrying out the integral in Eq. (A7). In the $\Delta p_{\rm min} \to 0$ limit, we have η_s, $\eta_d \to 1$, and Eq. (A8) simplifies to the standard result from kinetic gas theory ($\Gamma = nA\overline{v}/\sqrt{2\pi}$) or scattering theory ($\Gamma = n\langle\sigma v\rangle$, where $\langle\cdots\rangle$ denotes a thermal average).

Equation (A8) and Eq. (A6) assume that all motion perpendicular to the sensor surface is detectable by the readout system. That is to say, the readout system detects all motion along $\hat{u}_\perp$, which can be the case for tethered devices. However, motion readout for a levitated sensor will occur along the principle axes of the levitating trap and the details of the experimental setup may prevent simultaneous readout along all three principle axes [30, 40]. To calculate the event rate along a trap axis for a levitated nanosphere, we must project the center-of-mass momentum transfer onto the principle axis of the trap before integrating Eq. (A5) over the sensor surface area. Taking the readout axis to be z' such that $\hat{u}_\perp.\hat{z}' = \cos\theta$ and substituting for Δp yields

$$\begin{aligned}\frac{d\Gamma}{d\Delta p_{z'}} = \frac{n_g\Delta p_{z'}}{2m_g^2}\left(\frac{1}{2\pi\overline{v}^2}\right)^{1/2}4\pi R^2\int_0^{\pi/2}\sec^2\theta\sin\theta\, e^{-\Delta p_{z'}^2\sec^2\theta/2m_g^2\overline{v}^2}\\ \times\left(1 + \frac{\sqrt{\pi}}{2}\left(\frac{\Delta p_{z'}\sec\theta}{m_g\overline{v}} - \frac{2m_g\overline{v}}{\Delta p_{z'}\sec\theta}\right)\mathrm{erf}\big(\Delta p_{z'}\sec\theta/2m_g\overline{v}\big)e^{\Delta p_{z'}^2\sec^2\theta/4m_g^2\overline{v}^2}\right)d\theta,\end{aligned} \tag{A10}$$

where R is the nanosphere radius and $\Delta p_{z'}$ is the momentum transfer along the z' axis. To our knowledge, the integral in Eq. (A10) does not have an analytic expression. Specifically, the term proportional to $\sec\theta$ must be integrated numerically. However, we can still calculate the total collision rate by integrating over $\Delta p_{z'}$ and switching the order of integration. The total collision rate is then

$$\begin{aligned}\Gamma\big|_{\Delta p_{z'}>\Delta p_{\rm min}} &= n_g\sqrt{8\pi}R^2\overline{v}\int_0^{\pi/2}\left(e^{-\Delta p_{\rm min}^2\sec^2\theta/2m_g^2\overline{v}^2} + \frac{\sqrt{\pi}\Delta p_{\rm min}\sec\theta}{2m_g\overline{v}}\mathrm{erf}\big(\frac{\Delta p_{\rm min}\sec\theta}{2m_g\overline{v}}\big)e^{-\Delta p_{\rm min}^2\sec^2\theta/4m_g^2\overline{v}^2}\right)\sin\theta\, d\theta\\ &= \frac{n_g A\overline{v}}{\sqrt{2\pi}}\eta_d'(\Delta p_{\rm min}),\end{aligned} \tag{A11}$$

where the integral term defines the projected momentum cutoff for diffuse scattering $\eta_d'(\Delta p_{\rm min})$.

For specular scattering, the integral for event rate along a single trap axis is analytic, so the event rate is given by

$$\begin{aligned}\frac{d\Gamma}{d\Delta p_{z'}} &= \frac{n_g \Delta p_{z'}}{4m_g^2}\left(\frac{1}{2\pi\overline{v}^2}\right)^{1/2} \\ &\quad \times 4\pi R^2 \int_0^{\pi/2} \sec^2\theta \sin\theta\, e^{-\Delta p_{z'}^2 \sec^2\theta / 8m_g^2\overline{v}^2} d\theta \\ &= \frac{n_g \pi R^2}{m_g} \mathrm{erfc}\big(\frac{\Delta p_{z'}}{\sqrt{8} m_g \overline{v}}\big),\end{aligned} \tag{A12}$$

where erfc is the complementary Gaussian error function. The total collision rate for specular scattering is then

$$\begin{aligned}\Gamma\big|_{\Delta p_{z'} > \Delta p_{\min}} &= \frac{n_g \pi R^2}{m_g} \int_{\Delta p_{\min}}^{\infty} \mathrm{erfc}\big(\frac{\Delta p_{z'}}{\sqrt{8} m_g \overline{v}}\big) d\Delta p_{z'} \\ &= \frac{n_g A \overline{v}}{\sqrt{2\pi}} \eta_s'(\Delta p_{\min}).\end{aligned} \tag{A13}$$

where

$$\begin{aligned}\eta_s'(\Delta p_{\min}) &= e^{-\Delta p_{\min}^2 / 8 m_g^2 \overline{v}^2} \\ &\quad - \frac{\sqrt{\pi}\Delta p_{\min}}{\sqrt{8} m_g \overline{v}} \mathrm{erfc}\Big(\Delta p_{\min} / \sqrt{8} m_g \overline{v}\Big).\end{aligned} \tag{A14}$$

Appendix B: Scattering rates out of thermal equilibrium

When the sensor is not in thermal equilibrium with the background gas, then Eq. (A1) is modified to read

$$\begin{aligned}d^8 N_c(\vec{v}_i, \vec{v}_o) &= n_g\, dA\, dt \left(\frac{1}{2\pi\overline{v}^2}\right)^{3/2} v_i \cos\theta_i\, e^{-v_i^2/2\overline{v}^2} \\ &\times \frac{1}{2\pi\overline{v}_s^4} v_o \cos\theta_o\, e^{-v_o^2/2\overline{v}_s^2} d\vec{v}_i d\vec{v}_o,\end{aligned} \tag{B1}$$

where $\overline{v}_s = \sqrt{k_B T_s / m_g}$ is the root-mean-square thermal velocity of the diffusely scattered gas at the temperature of the sensor T_s.

Once again, we transform to Cartesian coordinates, impose the momentum transfer constraint, and evaluate the integrals over the plane parallel to the surface to find

$$\begin{aligned}d^3 N_c(\Delta p) = &\ \frac{n_g\, dA\, dt}{\overline{v}_s^2}\left(\frac{1}{2\pi\overline{v}^2}\right)^{1/2} \frac{d\Delta p}{m_g} \\ &\times \int_0^{\Delta p/m_g} dv_{i,z}\, v_{i,z} (\Delta p/m_g - v_{i,z}) \\ &\times e^{-v_{i,z}^2/2\overline{v}^2}\, e^{-(\Delta p/m_g - v_{i,z})^2/2\overline{v}_s^2}.\end{aligned} \tag{B2}$$

Completing the square in Eq. (B2) and mapping onto known Gaussian integrals yields

$$\begin{aligned}\frac{d^3 N_c(\Delta p)}{dA\, dt} = n_g \frac{d\Delta p}{m_g}\left(\frac{1}{2\pi\overline{v}^2}\right)^{1/2} &\frac{\overline{v}^2}{\left(\overline{v}^2 + \overline{v}_s^2\right)^2}\left(\frac{\Delta p}{m_g}\left(\overline{v}^2 e^{-\Delta p^2/2m_g^2\overline{v}^2} + \overline{v}_s^2 e^{-\Delta p^2/2m_g^2\overline{v}_s^2}\right)\right. \\ &\left. + \frac{\sqrt{\pi}}{2}\frac{\sqrt{2}\overline{v}\overline{v}_s}{\sqrt{\overline{v}^2 + \overline{v}_s^2}}\left(\frac{\Delta p^2}{m_g^2} - \overline{v}^2 - \overline{v}_s^2\right)\left(\mathrm{erf}\left(\frac{\Delta p\, \overline{v}_s}{m_g \overline{v}\sqrt{2(\overline{v}^2 + \overline{v}_s^2)}}\right) + \mathrm{erf}\left(\frac{\Delta p\, \overline{v}}{m_g \overline{v}_s \sqrt{2(\overline{v}^2 + \overline{v}_s^2)}}\right)\right) e^{-\Delta p^2/2m_g^2(\overline{v}^2 + \overline{v}_s^2)}\right).\end{aligned} \tag{B3}$$

After integrating over the sensor area, the differential event rate is

$$\frac{d\Gamma}{d\Delta p} = \frac{n_g A \Delta p}{m_g^2}\left(\frac{1}{2\pi\overline{v}^2}\right)^{1/2}\frac{\overline{v}^2}{\left(\overline{v}^2+\overline{v}_s^2\right)^2}\Bigg(\overline{v}^2 e^{-\Delta p^2/2m_g^2\overline{v}^2} + \overline{v}_s^2 e^{-\Delta p^2/2m_g^2\overline{v}_s^2} + \frac{\sqrt{\pi}}{2}\frac{\sqrt{2}\overline{v}\overline{v}_s}{\sqrt{\overline{v}^2+\overline{v}_s^2}}\Big(\frac{\Delta p}{m_g} - \frac{m_g(\overline{v}^2+\overline{v}_s^2)}{\Delta p}\Big)\Big(\mathrm{erf}\Big(\frac{\Delta p\,\overline{v}_s}{m_g\overline{v}\sqrt{2(\overline{v}^2+\overline{v}_s^2)}}\Big) + \mathrm{erf}\Big(\frac{\Delta p\,\overline{v}}{m_g\overline{v}_s\sqrt{2(\overline{v}^2+\overline{v}_s^2)}}\Big)\Big)e^{-\Delta p^2/2m_g^2(\overline{v}^2+\overline{v}_s^2)}\Bigg), \tag{B4}$$

and the total collision rate is

$$\begin{aligned}\Gamma\big|_{\Delta p>\Delta p_{\min}} = \frac{n_g A\overline{v}}{\sqrt{2\pi}}\frac{1}{\left(\overline{v}^2+\overline{v}_s^2\right)^2}\Bigg(&\overline{v}^4 e^{-\Delta p_{\min}^2/2m_g^2\overline{v}^2} + \overline{v}_s^4 e^{-\Delta p_{\min}^2/2m_g^2\overline{v}_s^2} \\ &+ \overline{v}^2\overline{v}_s^2 e^{-\Delta p_{\min}^2/2m_g^2(\overline{v}^2+\overline{v}_s^2)}\Big(e^{-\Delta p_{\min}^2\overline{v}_s^2/2m_g^2\overline{v}^2(\overline{v}^2+\overline{v}_s^2)} + e^{-\Delta p_{\min}^2\overline{v}^2/2m_g^2\overline{v}_s^2(\overline{v}^2+\overline{v}_s^2)}\Big) \\ &+ \frac{\sqrt{\pi}\overline{v}\overline{v}_s\Delta p_{\min}}{\sqrt{2}m_g}\sqrt{\overline{v}^2+\overline{v}_s^2}\Big(\mathrm{erf}\Big(\frac{\Delta p_{\min}\,\overline{v}_s}{m_g\overline{v}\sqrt{2(\overline{v}^2+\overline{v}_s^2)}}\Big) + \mathrm{erf}\Big(\frac{\Delta p_{\min}\,\overline{v}}{m_g\overline{v}_s\sqrt{2(\overline{v}^2+\overline{v}_s^2)}}\Big)\Big)e^{-\Delta p_{\min}^2/2m_g^2(\overline{v}^2+\overline{v}_s^2)}\Bigg).\end{aligned} \tag{B5}$$

When $T_s = T_{\mathrm{gas}}$, Eq. (B4) and Eq. (B5) reduce to Eq. (A6) and Eq. (A7), respectively.

To understand out-of-equilibrium operation when the motion readout of the optomechanical sensor occurs only along one axis, we project the center-of-mass momentum transfer onto the principle axis of the trap before integrating Eq. (B3) over the sensor surface area. Again taking the readout axis to be z' such that $\hat{u}_\perp.\hat{z}' = \cos\theta$ and substituting for Δp yields

$$\begin{aligned}\frac{d\Gamma}{d\Delta p_{z'}} = &\frac{n_g 4\pi R^2}{m_g}\left(\frac{1}{2\pi\overline{v}^2}\right)^{1/2}\frac{\overline{v}^2}{\left(\overline{v}^2+\overline{v}_s^2\right)^2}\int_0^{\pi/2}\sec^2\theta\sin\theta\,d\theta\Big(\frac{\Delta p_{z'}}{m_g}\Big(\overline{v}^2 e^{-\Delta p_{z'}^2\sec^2\theta/2m_g^2\overline{v}^2} + \overline{v}_s^2 e^{-\Delta p_{z'}^2\sec^2\theta/2m_g^2\overline{v}_s^2}\Big) \\ &+ \frac{\sqrt{\pi}\overline{v}\overline{v}_s}{\sqrt{2(\overline{v}^2+\overline{v}_s^2)}}\Big(\frac{\Delta p_{z'}^2}{m_g^2} - \frac{\overline{v}^2+\overline{v}_s^2}{\sec^2\theta}\Big)\sec\theta \\ &\times\Big(\mathrm{erf}\Big(\frac{\Delta p_{z'}\sec\theta\,\overline{v}_s}{m_g\overline{v}\sqrt{2(\overline{v}^2+\overline{v}_s^2)}}\Big) + \mathrm{erf}\Big(\frac{\Delta p_{z'}\sec\theta\,\overline{v}}{m_g\overline{v}_s\sqrt{2(\overline{v}^2+\overline{v}_s^2)}}\Big)\Big)e^{-\Delta p_{z'}^2\sec^2\theta/2m_g^2(\overline{v}^2+\overline{v}_s^2)}\Big) \\ = &\frac{n_g 4\pi R^2}{m_g}\left(\frac{1}{2\pi\overline{v}^2}\right)^{1/2}\frac{\overline{v}^2}{\left(\overline{v}^2+\overline{v}_s^2\right)^2}\sqrt{\frac{\pi}{2}}\Bigg(\Big(\overline{v}^3\mathrm{erfc}\Big(\frac{\Delta p_{z'}}{\sqrt{2}m_g\overline{v}}\Big) + \overline{v}_s^3\mathrm{erfc}\Big(\frac{\Delta p_{z'}}{\sqrt{2}m_g\overline{v}_s}\Big)\Big) \\ &+ \overline{v}\overline{v}_s\Big(\overline{v}\,\mathrm{erfc}\Big(\frac{\Delta p_{z'}}{\sqrt{2}m_g\overline{v}_s}\Big) + \overline{v}_s\mathrm{erfc}\Big(\frac{\Delta p_{z'}}{\sqrt{2}m_g\overline{v}}\Big) \\ &+ \sqrt{\overline{v}^2+\overline{v}_s^2}\,e^{-\Delta p_{z'}^2/2m_g^2(\overline{v}^2+\overline{v}_s^2)}\Big(\mathrm{erf}\Big(\frac{\Delta p_{z'}\,\overline{v}_s}{m_g\overline{v}\sqrt{2(\overline{v}^2+\overline{v}_s^2)}}\Big) + \mathrm{erf}\Big(\frac{\Delta p_{z'}\,\overline{v}}{m_g\overline{v}_s\sqrt{2(\overline{v}^2+\overline{v}_s^2)}}\Big)\Big)\Big) \\ &- \int_0^{\pi/2}\tan\theta\,d\theta\,\overline{v}\,\overline{v}_s\sqrt{(\overline{v}^2+\overline{v}_s^2)}\Big(\mathrm{erf}\Big(\frac{\Delta p_{z'}\sec\theta\,\overline{v}_s}{m_g\overline{v}\sqrt{2(\overline{v}^2+\overline{v}_s^2)}}\Big) + \mathrm{erf}\Big(\frac{\Delta p_{z'}\sec\theta\,\overline{v}}{m_g\overline{v}_s\sqrt{2(\overline{v}^2+\overline{v}_s^2)}}\Big)\Big)e^{-\Delta p_{z'}^2\sec^2\theta/2m_g^2(\overline{v}^2+\overline{v}_s^2)}\Bigg).\end{aligned} \tag{B6}$$

Again, the term proportional to $\sec\theta$ must be integrated numerically, but it is no longer amenable to reversing the order of integration. By integrating over $\Delta p_{z'}$, we arrive at the total collision rate

$$\begin{aligned}\Gamma\big|_{\Delta p_{z'}>\Delta p_{\min}} = &\frac{n_g A\overline{v}}{\sqrt{2\pi}}\frac{1}{\overline{v}^2+\overline{v}_s^2}\Bigg(\overline{v}^2 e^{-\Delta p_{\min}^2/2m_g^2\overline{v}^2} + \overline{v}_s^2 e^{-\Delta p_{\min}^2/2m_g^2\overline{v}_s^2} - \sqrt{\frac{\pi}{2}}\Delta p_{\min}\Big(\overline{v}\,\mathrm{erfc}\Big(\frac{\Delta p_{\min}}{\sqrt{2}m_g\overline{v}}\Big) + \overline{v}_s\mathrm{erfc}\Big(\frac{\Delta p_{\min}}{\sqrt{2}m_g\overline{v}_s}\Big)\Big) \\ &+ \sqrt{\frac{\pi}{2}}\frac{\overline{v}\,\overline{v}_s}{\sqrt{(\overline{v}^2+\overline{v}_s^2)}}\int_{\Delta p_{\min}}^{\infty}\Big(e^{-\Delta p_{z'}^2/2m_g^2(\overline{v}^2+\overline{v}_s^2)}\Big(\mathrm{erf}\Big(\frac{\Delta p_{z'}\,\overline{v}_s}{m_g\overline{v}\sqrt{2(\overline{v}^2+\overline{v}_s^2)}}\Big) + \mathrm{erf}\Big(\frac{\Delta p_{z'}\,\overline{v}}{m_g\overline{v}_s\sqrt{2(\overline{v}^2+\overline{v}_s^2)}}\Big)\Big) \\ &- \int_0^{\pi/2} e^{-\Delta p_{z'}^2\sec^2\theta/2m_g^2(\overline{v}^2+\overline{v}_s^2)}\Big(\mathrm{erf}\Big(\frac{\Delta p_{z'}\sec\theta\,\overline{v}_s}{m_g\overline{v}\sqrt{2(\overline{v}^2+\overline{v}_s^2)}}\Big) + \mathrm{erf}\Big(\frac{\Delta p_{z'}\sec\theta\,\overline{v}}{m_g\overline{v}_s\sqrt{2(\overline{v}^2+\overline{v}_s^2)}}\Big)\Big)\tan\theta\,d\theta\Big)d\Delta p_{z'}.\end{aligned} \tag{B7}$$

where the integral term defines the projected momentum cutoff for diffuse scattering $\eta_d'(\Delta p_{\min})$.

Appendix C: Uncertainty due to T_s and α

Using Eq. (B5) and Eq. (B7), we can calculate the variation in η_d and η_d' as a function of sensor surface temperature T_s, respectively. We can use the calculated

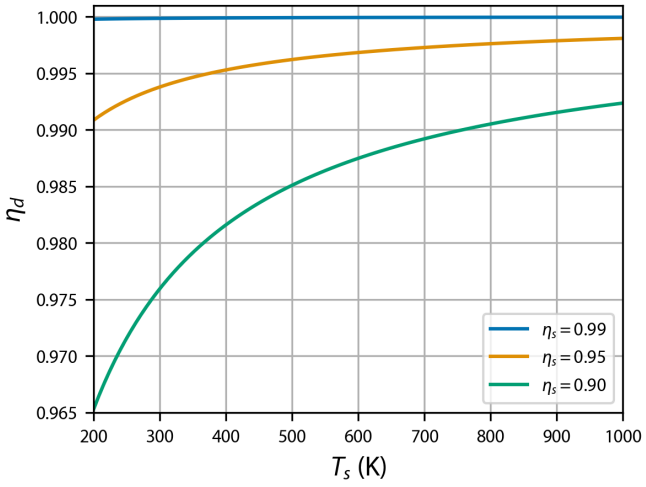

FIG. 3. Diffuse momentum cutoff η_d for a tethered sensor as a function of T_s for various values of η_s.

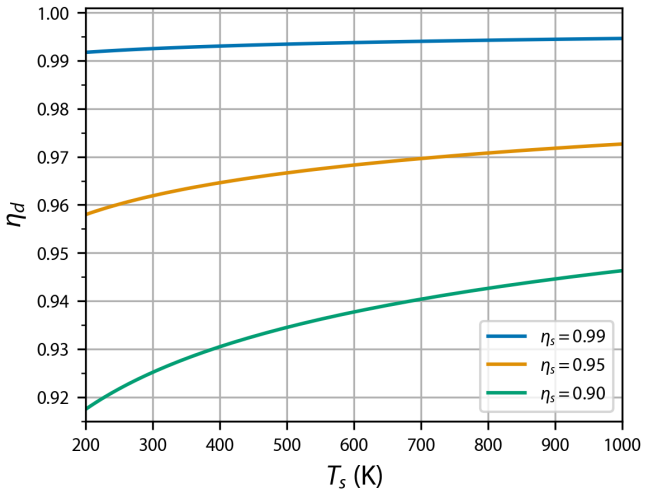

FIG. 4. Diffuse momentum cutoff η_d' for a nanosphere as a function of T_s for various values of η_s'.

change in η_d with T_s to estimate the uncertainty in a pressure measurement due to T_s, since T_s only enters Eq. (11) in the main text through η_d. Figure 3 shows the calculated η_d for H_2 gas colliding with a tethered sensor at each of $\eta_s = \{0.99, 0.95, 0.9\}$, which correspond to $\Delta p_{\min} = \{1.7, 4.4, 6.3\}$ keV/c. Because H_2 is the lightest gas, the results of Fig 3 represent a worst case scenario for a given $\Delta p_{\min}$. The change in η_d with T_s ranging from 200 K to 1000 K is less than 1 % for $\Delta p_{\min} < 4.4$ keV/c. When $\Delta p_{\min} = 6.3$ keV/c, the change in η_d with T_s from 200 K to 1000 K is still less than 3 %. Figure 4 shows the calculated η_d' for a nanosphere at each of $\eta_s' = \{0.99, 0.95, 0.9\}$, which correspond to $\Delta p_{\min} = \{0.11, 0.56, 1.1\}$ keV/c. When $\Delta p_{\min} = 1.1$ keV/c, the change in η_d' with T_s from 200 K to 1000 K is roughly 3 %. It appears that measuring the sensor surface temperature is not necessary for better than 5 % uncertainty pressure measurements, provided the sensor achieves a $\Delta p_{\min}$ such that $\eta_s > 0.9$.

A key feature of our proposal is that the measured pressure does not depend on the momentum accommodation coefficient α when $\eta_s \to 1$ and $\eta_d \to 1$ (*i.e.* $\Delta p_{\min} \to 0$). Given that $\Delta p_{\min} = 0$ is not experimentally achievable, we must assess the systematic uncertainty δP in the pressure measurement due to uncertainty $\delta\alpha$ in α. Applying linear error propagation theory, we find the fractional uncertainty in P due to α

$$\left(\frac{\delta P}{P}\right)_\alpha = \left|\frac{\eta_d - \eta_s}{\eta_s + \alpha(\eta_d - \eta_s)}\delta\alpha\right|. \tag{C1}$$

To apply Eq. (C1), we must estimate α and $\delta\alpha$. We can approximate α by finding the fraction of the Maxwell-Boltzmann distribution of the gas that has a de Broglie wavelength smaller than the characteristic surface roughness of the sensor. As a worst case, we can then take the true α to be uniformly distributed about the Maxwell-Boltzmann approximated mean value with a half-width that extends to the nearest edge of the physical range for α ($\alpha = 0$ or $\alpha = 1$). A completely uninformed prior on α then corresponds to a mean α of 0.5. Figure 5 shows the resulting $(\delta P/P)_\alpha$ as a function of α for a tethered sensor with $T_s = 300$ K. The estimated pressure measurement uncertainty is shown for $\eta_s = \{0.99, 0.95, 0.9, 0.75, 0.5\}$, which correspond to $\Delta p_{\min} = \{1.7, 4.4, 6.3, 10.5, 16.3\}$ keV/c. For $\eta_s > 0.9$ ($\Delta p_{\min} < 6.3$ keV/c), $(\delta P/P)_\alpha < 2.5$ %. Figure 6 shows the resulting $(\delta P/P)_\alpha$ as a function of α for a nanosphere with $T_s = 300$ K. Again, the estimated pressure measurement uncertainty is shown for $\eta_s = \{0.99, 0.95, 0.9, 0.75, 0.5\}$, which correspond to $\Delta p_{\min} = \{0.11, 0.56, 1.1, 3.0, 6.8\}$ keV/c. For $\eta_s > 0.9$ ($\Delta p_{\min} < 1.1$ keV/c), $(\delta P/P)_\alpha < 2.5$ %.

Armed with worst case estimates for uncertainty in $\delta\alpha$ and $\delta\eta_d$, we can estimate the total fractional pressure measurement uncertainty of our proposal. We will take the fractional uncertainty in the gas temperature $\delta T/T = 1$ %; the fractional uncertainty in the sensor area $\delta A/A = 2$ % [49]; and the fractional statistical uncertainty $\delta\Gamma|_{\Delta p > \Delta p_{\min}}/\Gamma|_{\Delta p > \Delta p_{\min}} = 1$ %. We will use the $\eta_s = 0.9$ worst case estimates from our analysis above for the uncertainties $\delta\alpha$ and $\delta\eta_d$. Adding all sources of uncertainty in quadrature yields $\delta P/P \approx 4.6$ % for either a tethered sensor or a nanosphere. Note that even modest improvements on our uncertainty estimates would yield fractional total uncertainties less than 2 %, which is state of the art for primary UHV metrology [25]. Such improvements could include improving $\Delta p_{\min}$ to reach $\eta_s = 0.95$; using heat transfer modeling or secondary thermometers to constrain T_s (even $\delta T_s \approx 100$ K would substantially reduce $\delta P/P$); and using the surface roughness of the sensor to estimate α as described above.

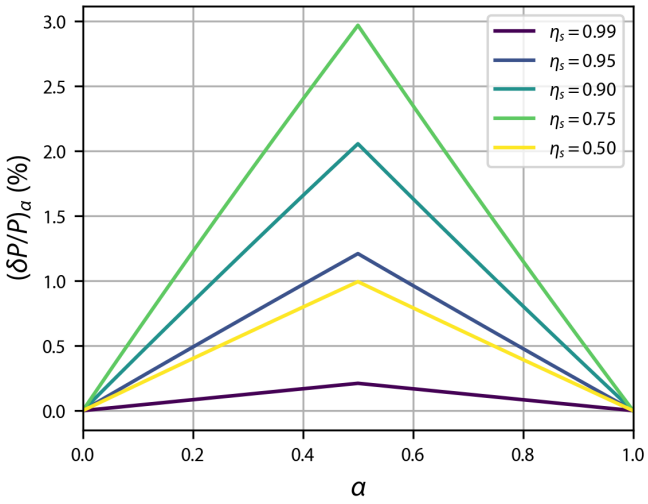

FIG. 5. Fractional pressure uncertainty $(\delta P/P)_\alpha$ due to uncertainty in α as a function of α for a tethered sensor at various values of η_s.

Appendix D: Ratiometric primary operation

In the main text, we required both $\eta_s \approx 1$ and $\eta_d \approx 1$ to ensure that incomplete momentum accommodation did not prevent primary pressure sensing. However, even when the detectable momentum cutoffs are significantly less than one, primary operation can be recovered ratiometrically if a single gas species has $\alpha = 0$ or $\alpha = 1$. There are two possible gas/sensor pairs where $\alpha = 0$ or $\alpha = 1$ might arise. First, collisions of xenon with a nanosphere with 1 nm surface roughness will be approximately 98% diffuse [53]. Second, collisions of H_2 or helium with an ultraflat tethered 2D material will be greater than 99% specular [54]. In either case, template momentum spectra for other gases can be built up ratiometrically using a classical pressure standard to transfer SI traceability [11]. A library of template momentum spectra can then be constructed to enable gas analysis beyond the $\alpha = 1$ limit.

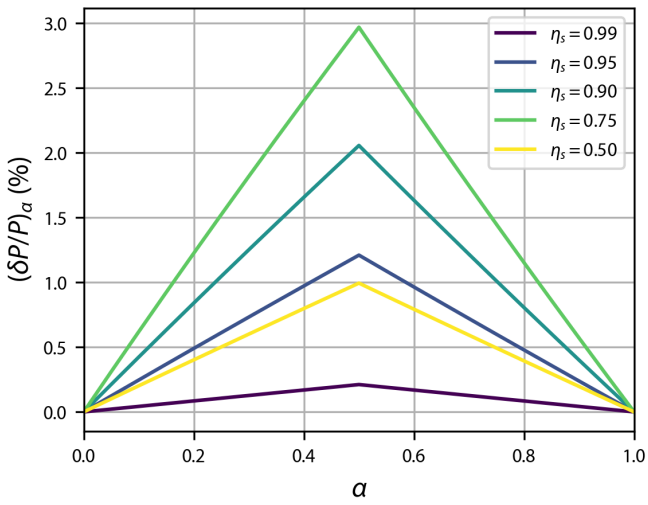

FIG. 6. Fractional pressure uncertainty $(\delta P/P)_\alpha$ due to uncertainty in α as a function of α for a nanosphere at various values of η_s'.

[1] R. Brown, "A brief account of microscopical observations made in the months of june, july and august 1827, on the particles contained in the pollen of plants; and on the general existence of active molecules in organic and inorganic bodies," The Philosophical Magazine **4**, 161–173 (1828).

[2] A. Einstein, "Über die von der molekularkinetischen theorie der wärme geforderte bewegung von in ruhenden flüssigkeiten suspendierten teilchen," Annalen der Physik **322**, 549–560 (1905).

[3] T. Li, S. Kheifets, D. Medellin, and M. G. Raizen, "Measurement of the instantaneous velocity of a brownian particle," Science **328**, 1673–1675 (2010).

[4] R. Huang, I. Chavez, K. M. Taute, B. Lukić, S. Jeney, M. G. Raizen, and E.-L. Florin, "Direct observation of the full transition from ballistic to diffusive brownian motion in a liquid," Nature Physics **7**, 576–580 (2011).

[5] T. Franosch, M. Grimm, M. Belushkin, F. M. Mor, G. Foffi, L. Forró, and S. Jeney, "Resonances arising from hydrodynamic memory in brownian motion," Nature **478**, 85–88 (2011).

[6] M. Blencowe, "Quantum electromechanical systems," Physics Reports **395**, 159–222 (2004).

[7] T. J. Kippenberg and K. J. Vahala, "Cavity optomechanics: back-action at the mesoscale," Science **321**, 1172–1176 (2008).

[8] M. Aspelmeyer, T. J. Kippenberg, and F. Marquardt, "Cavity optomechanics," Reviews of Modern Physics **86**, 1391 (2014).

[9] A. A. Clerk, M. H. Devoret, S. M. Girvin, F. Marquardt, and R. J. Schoelkopf, "Introduction to quantum noise, measurement, and amplification," Reviews of Modern Physics **82**, 1155 (2010).

[10] P. A. Redhead, Extreme high vacuum, Tech. Rep. (CERN, 1999).

[11] J. Scherschligt, J. A. Fedchak, D. S. Barker, S. Eckel, N. Klimov, C. Makrides, and E. Tiesinga, "Development of a new UHV/XHV pressure standard (cold atom vacuum standard)," Metrologia **54**, S125 (2017).

[12] L. H. Ehinger, B. P. Acharya, D. S. Barker, J. A. Fedchak, J. Scherschligt, E. Tiesinga, and S. Eckel, "Comparison of two multiplexed portable cold-atom vacuum standards," AVS Quantum Sci. **4**, 034403 (2022).

[13] G. Gabrielse, X. Fei, L. Orozco, R. Tjoelker, J. Haas, H. Kalinowsky, T. Trainor, and W. Kells, "Thousandfold improvement in the measured antiproton mass," Physical

review letters **65**, 1317 (1990).
[14] R. Kaltenbaek, G. Hechenblaikner, N. Kiesel, O. Romero-Isart, K. C. Schwab, U. Johann, and M. Aspelmeyer, "Macroscopic quantum resonators (maqro) testing quantum and gravitational physics with massive mechanical resonators," Experimental Astronomy **34**, 123–164 (2012).
[15] S. Bose, A. Mazumdar, G. W. Morley, H. Ulbricht, M. Toroš, M. Paternostro, A. A. Geraci, P. F. Barker, M. Kim, and G. Milburn, "Spin entanglement witness for quantum gravity," Physical Review Letters **119**, 240401 (2017).
[16] D. Carney, P. C. E. Stamp, and J. M. Taylor, "Tabletop experiments for quantum gravity: a user's manual," Classical and Quantum Gravity **36**, 034001 (2019).
[17] D. Carney, K. G. Leach, and D. C. Moore, "Searches for massive neutrinos with mechanical quantum sensors," (2022), arXiv:2207.05883 [hep-ex].
[18] J. Zhang, G. Pagano, P. W. Hess, A. Kyprianidis, P. Becker, H. Kaplan, A. V. Gorshkov, Z.-X. Gong, and C. Monroe, "Observation of a many-body dynamical phase transition with a 53-qubit quantum simulator," Nature **551**, 601–604 (2017).
[19] G. Pagano, P. Hess, H. Kaplan, W. Tan, P. Richerme, P. Becker, A. Kyprianidis, J. Zhang, E. Birckelbaw, M. Hernandez, et al., "Cryogenic trapped-ion system for large scale quantum simulation," Quantum Science and Technology **4**, 014004 (2018).
[20] C. J. Riedel, "Direct detection of classically undetectable dark matter through quantum decoherence," Physical Review D **88**, 116005 (2013).
[21] D. Carney, S. Ghosh, G. Krnjaic, and J. M. Taylor, "Proposal for gravitational direct detection of dark matter," Phys. Rev. D **102**, 072003 (2020), arXiv:1903.00492 [hep-ph].
[22] D. Carney, G. Krnjaic, D. C. Moore, C. A. Regal, G. Afek, S. Bhave, B. Brubaker, T. Corbitt, J. Cripe, N. Crisosto, et al., "Mechanical quantum sensing in the search for dark matter," Quantum Science and Technology **6**, 024002 (2021).
[23] G. Afek, D. Carney, and D. C. Moore, "Coherent scattering of low mass dark matter from optically trapped sensors," Physical Review Letters **128**, 101301 (2022).
[24] J. A. Fedchak, P. J. Abbott, J. H. Hendricks, P. C. Arnold, and N. T. Peacock, "Review article: Recommended practice for calibrating vacuum gauges of the ionization type," Journal of Vacuum Science and Technology A: Vacuum, Surfaces, and Films **36**, 030802 (2018).
[25] D. S. Barker, J. A. Fedchak, J. Kłos, J. Scherschligt, A. A. Sheikh, E. Tiesinga, and S. P. Eckel, "Accurate measurement of the loss rate of cold atoms due to background gas collisions for the quantum-based cold atom vacuum standard," AVS Quantum Science **5**, 035001 (2023).
[26] A. Clerk, "Quantum-limited position detection and amplification: A linear response perspective," Physical Review B **70**, 245306 (2004).
[27] S. Ghosh, D. Carney, P. Shawhan, and J. M. Taylor, "Backaction-evading impulse measurement with mechanical quantum sensors," Physical Review A **102**, 023525 (2020).
[28] U. Delić, M. Reisenbauer, K. Dare, D. Grass, V. Vuletić, N. Kiesel, and M. Aspelmeyer, "Cooling of a levitated nanoparticle to the motional quantum ground state," Science **367**, 892–895 (2020).
[29] F. Tebbenjohanns, M. L. Mattana, M. Rossi, M. Frimmer, and L. Novotny, "Quantum control of a nanoparticle optically levitated in cryogenic free space," Nature **595**, 378–382 (2021).
[30] L. Magrini, P. Rosenzweig, C. Bach, A. Deutschmann-Olek, S. G. Hofer, S. Hong, N. Kiesel, A. Kugi, and M. Aspelmeyer, "Real-time optimal quantum control of mechanical motion at room temperature," Nature **595**, 373–377 (2021).
[31] Z.-Q. Yin, A. A. Geraci, and T. Li, "Optomechanics of levitated dielectric particles," International Journal of Modern Physics B **27**, 1330018 (2013).
[32] J. Millen, T. S. Monteiro, R. Pettit, and A. N. Vamivakas, "Optomechanics with levitated particles," Reports on Progress in Physics **83**, 026401 (2020).
[33] D. C. Moore and A. A. Geraci, "Searching for new physics using optically levitated sensors," Quantum Science and Technology **6**, 014008 (2021).
[34] P.-L. Yu, K. Cicak, N. Kampel, Y. Tsaturyan, T. Purdy, R. Simmonds, and C. Regal, "A phononic bandgap shield for high-q membrane microresonators," Applied Physics Letters **104**, 023510 (2014).
[35] J. N. Kirchhof, K. Weinel, S. Heeg, V. Deinhart, S. Kovalchuk, K. Höflich, and K. I. Bolotin, "Tunable Graphene Phononic Crystal," Nano Lett. **21**, 2174 (2021).
[36] A. Jayich, J. Sankey, B. Zwickl, C. Yang, J. Thompson, S. Girvin, A. Clerk, F. Marquardt, and J. Harris, "Dispersive optomechanics: a membrane inside a cavity," New Journal of Physics **10**, 095008 (2008).
[37] J. S. Bunch, A. M. Van Der Zande, S. S. Verbridge, I. W. Frank, D. M. Tanenbaum, J. M. Parpia, H. G. Craighead, and P. L. McEuen, "Electromechanical resonators from graphene sheets," Science **315**, 490–493 (2007).
[38] B. Zwickl, W. Shanks, A. Jayich, C. Yang, A. Bleszynski Jayich, J. Thompson, and J. Harris, "High quality mechanical and optical properties of commercial silicon nitride membranes," Applied Physics Letters **92**, 103125 (2008).
[39] D. J. Wilson, C. A. Regal, S. B. Papp, and H. Kimble, "Cavity optomechanics with stoichiometric sin films," Physical review letters **103**, 207204 (2009).
[40] F. Monteiro, G. Afek, D. Carney, G. Krnjaic, J. Wang, and D. C. Moore, "Search for composite dark matter with optically levitated sensors," Physical Review Letters **125**, 181102 (2020).
[41] S. Knapen, T. Lin, M. Pyle, and K. M. Zurek, "Detection of Light Dark Matter With Optical Phonons in Polar Materials," Phys. Lett. B **785**, 386–390 (2018), arXiv:1712.06598 [hep-ph].
[42] N. F. Ramsay, Molecular Beams (Oxford University Press Inc., New York, 1956).
[43] A. Cavalleri, G. Ciani, R. Dolesi, M. Hueller, D. Nicolodi, D. Tombolato, S. Vitale, P. J. Wass, and W. J. Weber, "Gas damping force noise on a macroscopic test body in an infinite gas reservoir," Phys. Lett. A **374**, 3365 (2010).
[44] L. Martinetz, K. Hornberger, and B. A. Stickler, "Gas-induced friction and diffusion of rigid rotors," Phys. Rev. E **97**, 052112 (2018).
[45] C. P. Blakemore, D. Martin, A. Fieguth, A. Kawasaki, N. Priel, A. D. Rider, and G. Gratta, "Absolute pressure and gas species identification with an optically levitated rotor," J. Vac. Sci. Technol. B **38**, 024201 (2020).

[46] J. K. Fremerey, "The spinning rotor gauge," J. Vac. Sci. Technol. A **3**, 1715 (1985).

[47] C. R. Tilford, "Pressure and Vacuum Measurements," in Phys. Methods Chem., Vol. 6, edited by B. W. Rossiter and R. C. Baetzold (John Wiley and Sons, Inc., 1992) 2nd ed., pp. 101–173.

[48] J. Scherschligt, J. A. Fedchak, Z. Ahmed, D. S. Barker, K. Douglass, S. Eckel, E. Hanson, J. Hendricks, N. Klimov, T. Purdy, J. Ricker, R. Singh, and J. Stone, "Review Article: Quantum-based vacuum metrology at the National Institute of Standards and Technology," J. Vac. Sci. Technol. A **36**, 040801 (2018).

[49] C. P. Blakemore, A. D. Rider, S. Roy, A. Fieguth, A. Kawasaki, N. Priel, and G. Gratta, "Precision mass and density measurement of individual optically levitated microspheres," Phys. Rev. Appl. **12**, 024037 (2019).

[50] T. P. Purdy, K. E. Grutter, K. Srinivasan, and J. M. Taylor, "Quantum correlations from a room-temperature optomechanical cavity," Science **356**, 1265 (2017).

[51] J. Xiao, T. Plaskocinski, M. Biabanifard, S. Persheyev, and A. D. Falco, "On-chip optical trapping with high NA metasurfaces," ACS Photonics **10**, 1341 (2023).

[52] A. Vinante, A. Pontin, M. Rashid, M. Toroš, P. F. Barker, and H. Ulbricht, "Testing collapse models with levitated nanoparticles: Detection challenge," Phys. Rev. A **100**, 012119 (2019).

[53] C. P. Hsu, S. N. Ramakrishna, M. Zanini, N. D. Spencer, and L. Isa, "Roughness-dependent tribology effects on discontinuous shear thickening," Proc. Natl. Acad. Sci. U. S. A. **115**, 5117 (2018).

[54] C. H. Lui, L. Liu, K. F. Mak, G. W. Flynn, and T. F. Heinz, "Ultraflat graphene," Nature **462**, 339 (2009).